Applied Energy 360 (2024) 122817

Contents lists available at ScienceDirect

Applied Energy

journal homepage: www.elsevier.com/locate/apenergy

# High-fidelity numerical simulations of a standing-wave thermoacoustic engine

Nathan Blanc [a,b], Michael Laufer [c], Steven Frankel [c], Guy Z. Ramon [a,b,*]

[a] *Grand Technion Energy Program, Haifa, 32000, Israel*
[b] *Faculty of Civil and Environmental Engineering, Technion, Haifa, 32000, Israel*
[c] *Faculty of Mechanical Engineering, Technion, Haifa, 32000, Israel*

## GRAPHICAL ABSTRACT

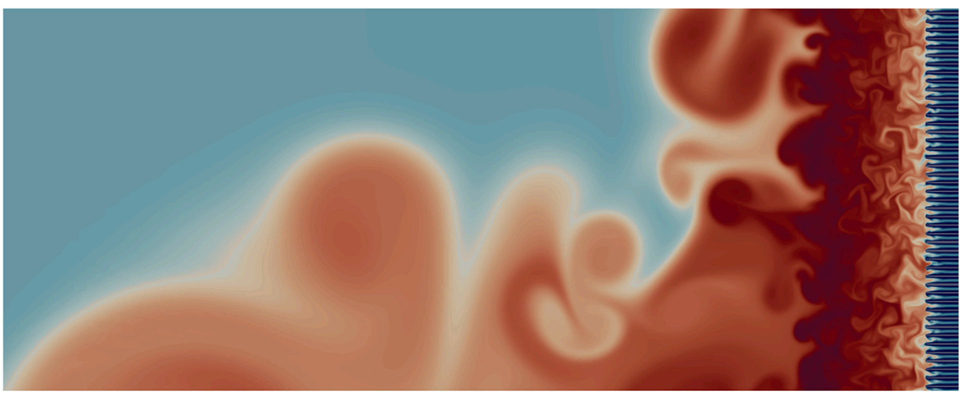

## ARTICLE INFO

*Keywords:*
Thermoacoustics
Thermoacoustic engine
High fidelity simulations
Non-linear thermoacoustics
Computational fluid dynamics

## ABSTRACT

Thermoacoustic devices, in which heat fluxes and pressure waves are converted from one to the other, are a promising class of energy conversion, particularly as heat-driven heat pumps. However, accurate simulation and performance prediction of these devices is a major challenge on the path to better understanding and improved design.

Herein, 2D simulations of a high-amplitude standing wave thermoacoustic engine are reported, based on the high-fidelity software PyFR. The performed simulations are validated against both computational and experimental results reported in the literature, exhibiting a deviation of less than 9% between the calculated and experimentally measured pressure amplitude, more than twice as accurate as previously reported calculations.

Further, non-linear effects in the thermoacoustic engine are explored and discussed, including Rayleigh streaming, jet streaming and, importantly, higher-order harmonics. The influence of these effects on engine performance is gauged, with higher-order harmonics shown to cause the greatest reduction in engine performance. Harmonics suppression is then demonstrated, via a simple example, to improve performance and, in the present context, greatly reduce the deviation between the linear and non-linear model.

This work demonstrates the utility of high-order CFD schemes for the analysis of thermoacoustics devices, providing useful insight on the importance of non-linear effects and highlighting the potential benefits of future work along similar lines.

* Corresponding author at: Grand Technion Energy Program, Haifa, 32000, Israel.
*E-mail address:* Ramong@technion.ac.il (G.Z. Ramon).

https://doi.org/10.1016/j.apenergy.2024.122817
Received 1 October 2023; Received in revised form 22 November 2023; Accepted 3 February 2024
Available online 21 February 2024
0306-2619/

## 1. Introduction

Thermoacoustic engines are a relatively new type of energy conversion device, transforming heat into acoustic power via thermal interactions in an acoustic wave. The generated acoustic power can be used, e.g., for electricity generation [1] and air compression [2]. The inverse operation, performed by thermoacoustic heat pumps, uses acoustic power to pump heat up a temperature gradient [3,4]. The integration of a thermoacoustic engine with a thermoacoustic heat pump provides a platform for a highly reliable, heat-driven cooling device, with no moving parts [5]. Thermoacoustic cooling technology has been used in space applications [6] and holds great promise for gas liquefaction [7] and waste heat recovery [8,9].

A key challenge for improving this technology, in an effort to increase efficiency and energy density, is accurate performance prediction, enabling iterative design and optimization. This requires mathematical models of thermoacoustic phenomena, which present a complex system due to the inherent non-linearity and strongly coupled physical mechanisms. Three prominent approaches have been demonstrated for such simulations. Due to the aforementioned inherent complexity, the most commonly used model for thermoacoustic devices is a 1D, linear, phasor model developed by Rott [10] and extended by Swift [11]. This model has been made accessible via the software DeltaEC [12], which is currently the standard tool used for thermoacoustic system design. Other computational tools based on the linear model include Thermoacoustica [13] Dstar [14] and, more recently, PC-TAS [15], which extends the scope to systems that include phase-change (see, for example, [16–18]). Calculations based on the linear model are typically executed quickly and with relative ease due to the simplifications made. While certain parameters (e.g. onset conditions, operating frequency) are well predicted by the linear model, its ability to accurately capture the pressure amplitude is limited to small amplitudes. Large deviations between simulation and experiments have been observed as the acoustic pressure amplitude becomes larger than 10% of the mean pressure [19], and sometimes even at values as small as 5% [20]. These deviations occur due to non-linear effects such as streaming, higher harmonics, turbulence, and end effects (e.g., jet formation in transition between segments of the resonator), none of which are captured by the linear model. Because the energy density of thermoacoustic devices is directly linked to the pressure amplitude, this renders the linear theory inapplicable for accurate prediction of performance for designing practical devices.

A more "straightforward" approach is the direct, full-scale simulation of the thermoacoustic device. Over the past 15 years, several studies have simulated full-scale thermoacoustic devices, in 2D as well as 3D (the interested reader is referred to [21] for a review of these. A detailed discussion is also given in Appendix A.2). However, none of these studies present proper validation of the numerical results against experimental measurements — most are not validated at all or validated against either other CFD results or calculations based on the linear model. Simulations that have been validated against experimental data have either presented large deviations (>20%) from experimental results (e.g. [22–24]), or else have shown good agreement only for parameters such as the frequency, onset characteristics, and pressure amplitudes at low drive ratios (e.g. [25–27]). These parameters are relatively easy to obtain numerically, as they do not require accurate resolution of non-linear effects. Indeed, for calculating these parameters the linear model is quite satisfactory, as has been extensively demonstrated by Swift [19]. To the best of our knowledge, an experimentally-validated, accurate, full-scale simulation of a thermoacoustic system has yet to be performed. We note that, while the aforementioned reports utilize low-order, commercial CFD schemes, there have been a few reports of self-developed codes, some of which employ high-fidelity methods. For example [28–30] used LES methods to simulate a standing wave engine, and [31,32] used a flux reconstruction method to simulate both standing and travelling wave engines. However, these have also not been validated against experimental results. A third, 'intermediate', approach has been used for resolving additional effects not captured by the linear model, without fully resolving the system. The Sage [33] and Regen3 [34] software packages use a transient 1D model, rather than seeking a solution in the frequency domain. Ahmed et al. [35], Boroujerdi and Ziabasharhagh [36], Sugimoto [37], Olivier et al. [38] and Abd El-Rahman and Abdel-Rahman [39] all followed similar methodologies, the latter obtaining good agreement with experimental data, even at high amplitudes outside the linear regime. Boroujerdi and Ziabasharhagh [40] also obtained reasonable agreement with experimental data by coupling a 2D model in the stack region with an intermediate model in the resonator region. However, the accuracy of these models strongly depends on correlations that average the effect of 2D thermoviscous behaviour on the 1D acoustic propagation. Abd El-Rahman and Abdel-Rahman [39] and Boroujerdi and Ziabasharhagh [40] both emphasized the importance of the proper choice of such correlations for accurate simulation. This makes these intermediate models prone to over-fitting of existing experimental results, and inaccurately capturing new configurations or situations.

It is, therefore, our purpose to present an accurate, high-fidelity simulation of a thermoacoustic engine, validated against experimental results.

## 2. Simulation details

### 2.1. Model setup

The system forming the base of the current computational work is the standing wave engine designed by Swift [20]. This configuration was chosen due to the availability of reliable experimental data, its relative simplicity, and the large reported deviation between its performance and the predictions of the linear model. The engine consists of a 5-inch diameter resonator, a Stainless steel honeycomb as the stack, and two heat exchangers. The resonator is filled with Helium at a mean pressure of $p_m = 13.8$ bar.

In our simulation, the system was modelled as a 2D scaled domain with a fully resolved porous region simulating the stack and heat exchangers (see Fig. 1**(B)** and Table 1 for system schematic and dimensions.). All dimensions were scaled by the length of the system, motivated by a previous Investigation of the same experimental system by Olson and Swift [41], who concluded that geometrical scaling does not affect system behaviour in terms of the oscillating pressure, temperature, and velocity fields. In addition, the frequency of the acoustic oscillation is expected to scale with system length.

We note that the actual geometry of the experimental system is three-dimensional and not fully represented by this model. Nevertheless, the hydraulic radius of the stack pores and the resonator, as well as the porosity (ratio of unobstructed area to full area) of the stack region, are maintained in the present model.

**Table 1**
Geometric dimensions corresponding with the symbols found in Fig. 1.

| Parameter | Value | Units |
|---|---|---|
| L | 1 | m |
| $L_1$ | 64.5 | mm |
| $L_{HHX}$ | 13.8 | mm |
| $L_{Stack}$ | 64.5 | mm |
| $L_{AHX}$ | 11.5 | mm |
| D | 29 | mm |
| $h_1$ | 205 | µm |
| $h_2$ | 50 | µm |

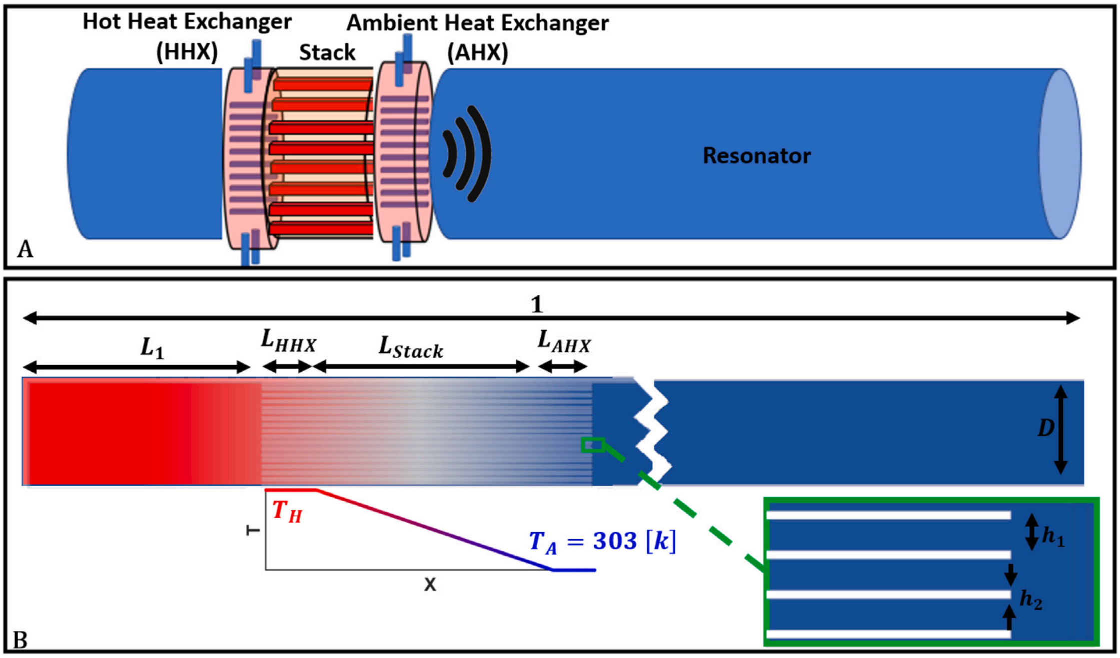


**Fig. 1.** **A:** Schematic of the standing wave engine studied by Swift [20]. A temperature gradient is imposed on the stack, leading to the spontaneous generation of acoustic waves in the resonator. **B:** The computational domain representing the engine - a duct with a fully resolved porous region. A no-slip, no-penetration boundary condition is imposed on all solid surfaces. Adiabatic conditions are imposed on all the surfaces except the porous region walls, on which a temperature profile is imposed, as presented in the figure. In the simulation, a small acoustic disturbance grows until a limit cycle is reached. Numerical values of the different geometric parameters can be found in Table 1.

### 2.2. Equations

Numerical experiments were conducted by solving the two-dimensional, compressible continuity, momentum and energy balance equations, presented here in conservative form:

$$\frac{\partial \rho}{\partial t} + \nabla \cdot (\rho \mathbf{u}) = 0 \tag{1}$$

$$\frac{\partial (\rho \mathbf{u})}{\partial t} + \nabla \cdot \left(\rho \mathbf{u} \otimes \mathbf{u}^T + p\mathbf{I} - \underline{\tau}\right) = 0, \tag{2}$$

$$\frac{\partial E}{\partial t} + \nabla \cdot \left(\mathbf{u}(p+E) - \mathbf{u} \cdot \underline{\tau} + \frac{\mu c_p}{Pr} \nabla T\right) = 0, \tag{3}$$

Where

$$\underline{\tau} = \mu \left[\nabla \mathbf{u} + \nabla(\mathbf{u}^T) - \frac{2}{3}(\nabla \cdot \mathbf{u})\mathbf{I}\right], \tag{4}$$

is the stress tensor, $\mathbf{u}, \rho, p, c_p, T, \mu$ and $Pr$ are the velocity vector, density, pressure, specific heat, temperature, dynamic viscosity and Prandtl number of the fluid, respectively. Furthermore, E denotes the total energy (kinetic and thermal) of the fluid per unit volume. Under the assumption of a perfect gas, $E$ and $T$ are given by

$$T = \frac{\gamma}{\gamma - 1} \frac{p}{\rho c_p}, \tag{5}$$

$$E = \frac{p}{\gamma - 1} + \frac{1}{2}\rho |\mathbf{u}|^2, \tag{6}$$

where $\gamma$ is the fluid's specific heat ratio.

We note that Eqs. (1)–(3) can be written in the form:

$$\frac{\partial B}{\partial t} + \nabla \cdot f(B, \nabla B) = 0 \tag{7}$$

Where B is a solution variable and f is the flux associated with the variable. This notation will be used in the description of the solver.

### 2.3. Solver

Eqs. (1)–(6) were solved using the open-source code PyFR [42], employs the flux-reconstruction (FR) method enabling arbitrary high-order function approximations [43]. FR is closely related to the discontinuous Galerkin method, which defines an interpolating polynomial for the solution and the flux using multiple solution points per element. The algorithm will be briefly described here, and the interested reader can find a detailed description in [42].

**Table 2**
Details of meshes used in simulation.

| | Mesh 1 (2D) | Mesh 2 (2D) | 3D |
|---|---|---|---|
| Mesh | Quadrangular | Quadrangular | Hexahedral |
| Number of elements | 200k | 270k | 2.9M |
| Number of DOF | 3M | 4.2M | 187M |

#### 2.3.1. Solution variable representation

After the physical domain is decomposed into elements (in other words, after a mesh is generated), any arbitrarily shaped element is mapped into a standard element in a transformed space with coordinates $0 \leq \tilde{\mathbf{x}} \leq 1$. The solution variable inside the element i is then represented by a linear combination of a set of nodal base functions

$$B_i(\tilde{\mathbf{x}}) = \sum_{j=1}^{n} B_{ij} L_j(\tilde{\mathbf{x}}) \tag{8}$$

Where i is the element number, j is an internal point number inside the element, $p_{ij}$ is the value of $p$ at the internal point j, and

$$L_k(\tilde{\mathbf{x}}) = \prod_{j=0, j \neq k}^{n} \frac{\tilde{\mathbf{x}} - \tilde{\mathbf{x}}_j}{\tilde{\mathbf{x}}_k - \tilde{\mathbf{x}}_j} \tag{9}$$

is a polynomial base function. The base functions are chosen so that $L_{ij}(\tilde{\mathbf{x}}_{ik}) = \delta_{jk}$ where $\delta$ is the kronecker delta function. $n$, the number of functions in the base, can be chosen at will, allowing for arbitrarily high-order spatial accuracy. In general, the computational cost in PyFR simulations is proportional to the number of degrees of freedom in the domain,

$$N_{DOF} = N_{elements} \cdot n. \tag{10}$$

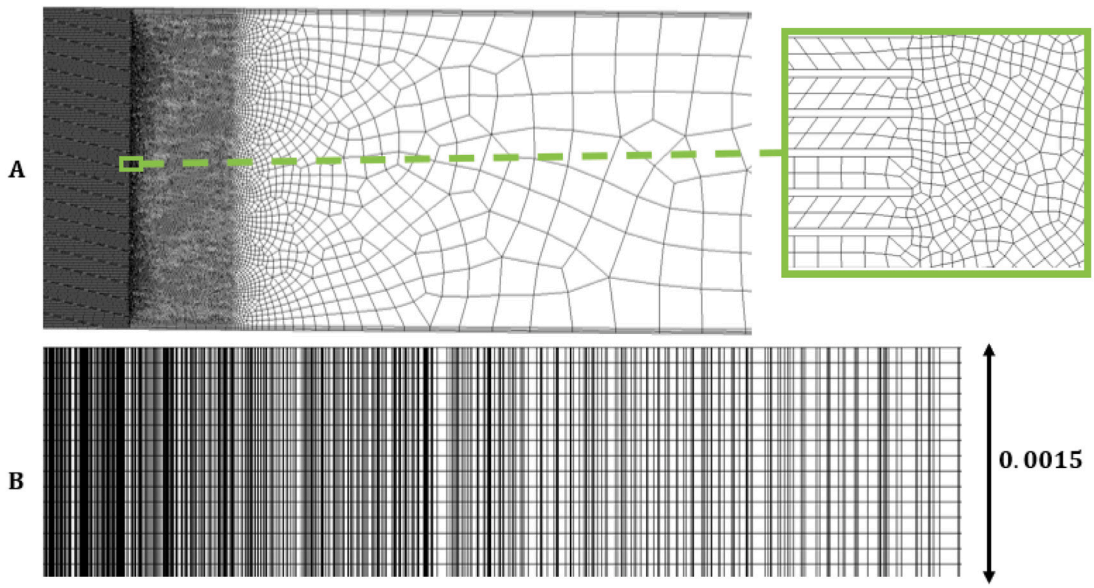


**Fig. 2. A:** The 2D mesh used for most simulations. **B:** Top view of the 3D mesh.

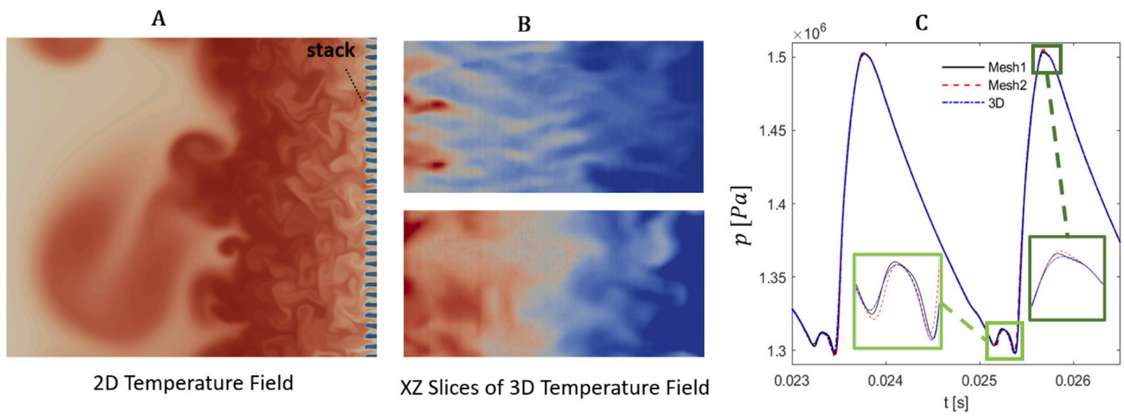


**Fig. 3. (A)**: Calculations of the 2D temperature field and complex flow structures created near the stack. **(B)**: Complex flow structures revealed via top slices of the 3D temperature field in the stack region at $y = 0.0149$. **(C)**: Comparison of the pressure amplitude calculated using the two different 2D meshes (see Table 2) and the 3D mesh. A 2D simulation with mesh 1 is sufficient to resolve the macroscopic features of the flow, as manifested through the oscillating pressure.

#### 2.3.2. Evaluation of flux divergence

For a solution variable B, the flux reconstruction algorithm is used to evaluate the flux divergence $\nabla \cdot f(B, \nabla B)$. The flux between two neighbouring elements is first calculated by using the polynomial approximation from Eq. (8):

$$\hat{f}_i^{\delta}(\tilde{\mathbf{x}}) = \sum_{j=0}^{n} f\left(B_i(x_j)\right) L_j(\tilde{\mathbf{x}}) \tag{11}$$

The values of the flux at the element boundaries for neighbouring elements will, in general, be discontinuous, and is therefore marked by the superscript $\delta$. An additional common interface flux is hence needed in order to maintain a conservative scheme. The value of this added flux, $\hat{f}_i^{num}$ is calculated using an approximate Riemann solver or a Local discontinuous Galerkin type method. The discontinuous flux is then corrected:

$$\frac{\partial \hat{f}}{\partial \tilde{\mathbf{x}}} = \frac{\partial \hat{f}^{\delta}}{\partial \tilde{\mathbf{x}}} + \left(\hat{f}_L^{num} - \hat{f}_L^{\delta}\right)\frac{dh_L}{d\tilde{\mathbf{x}}} + \left(\hat{f}_R^{num} - \hat{f}_R^{\delta}\right)\frac{dh_R}{d\tilde{\mathbf{x}}}, \tag{12}$$

Where h is a correction function of a polynomial order (n+1), and the subscripts R and L denote the two neighbouring elements. The correction function h is chosen so that $h_L(-1) = h_R(1) = 1$ and $h_L(1) = h_R(-1) = 0$. For additional details about the choice of h, see Ref. [44]. The corrected flux from Eq. (12) is now continous between different elements, and is then used to march forward in time using a numerical integrator (e.g. a Runge–Kutta integrator).

#### 2.3.3. Benefits of using PyFR

PyFR's scheme has been shown to outperform commercial CFD packages in terms of accuracy, while operating on fully unstructured meshes. [45]. Both numerical dissipation and dispersion are reduced, allowing to accurately capture intricate fluid phenomena. It is worth noting that PyFR is designed to run efficiently using graphics processing units (GPUs), while commercial CFD software packages are normally restricted to running on the CPU. On modern supercomputers, the majority of the computational power and available memory bandwidth is allocated to GPUs. The simulations in this work used The PyFR CUDA backend, along with the GiMMiK library to accelerate the sparse matrix multiplications resulting from the explicit integration and Flux Reconstruction approach. These features make PyFR well-suited for the problem at hand. All of our simulations were run with a solution order of 3, meaning the base functions were 3rd-order polynomials in all the spatial coordinates.

### 2.4. Boundary and initial conditions

No-penetration and no-slip boundary conditions ($\mathbf{u} = 0$) were imposed on all solid boundaries. Adiabatic conditions ($\nabla T = 0$) were imposed on the resonator walls, and the following temperature profile is imposed on the porous region,

$$\begin{cases} T = T_H & \text{HHX} \\ T = T_H + (T_A - T_H) X_{stack} & \text{Stack} \\ T = T_A = 303 \text{ K} & \text{AHX} \end{cases} \tag{13}$$

where $X_{stack}$ is the X coordinate relative to the beginning of the stack region. The initial conditions were defined as follows: a simulation at $T_H = 603$ K was performed with near quiescent initial conditions ($p \equiv p_m, u \equiv 0.1$ m/s), to observe the destabilization that occurs when beginning from a small initial disturbance. The rest of the simulations were conducted with an initial sinusoidal pressure distribution,

$$p = p_m + p_0 \sin(\pi X).$$

In order to converge to the limit cycle more quickly, $p_0$ was chosen based on a rough estimation of the projected limit cycle pressure amplitude. The boundary and initial conditions are further explained in the appendix (Table A.1 and Fig. A.1).

### 2.5. Additional simulation details

Values used in the simulations for the heat capacity, $c_p$, Prandtl number, $Pr$, and specific heat ratio, $\gamma$, were 5192 J/kg K, 0.67, and 1.6667, respectively, while the viscosity was modelled using Sutherland's ([46]) law:

$$\mu = \mu_0 \left(\frac{T}{T_0}\right)^{1.5} \frac{T_0 + S}{T + S}, \tag{14}$$

where $T_0 = 300$ [K] is the reference temperature, $\mu_0 = 4.6296$ Pa s is the viscosity at the reference temperature, and $S = 80$ K is a gas property.

Simulations were run using a discontinuous Galerkin scheme and a Rusanov Riemann solver for the interface flux (see [42] for details on interface flux calculations). Further, the upwind and penalty terms were set to $\beta = 1/2$ and $\tau = 1/10$, respectively. For the time integration, a Runge–Kutta 45 routine was utilized, with a variable time-step determined via a *pi* controller. The nominal time-step used was approximately $1e{-}10$ s, and the time steps chosen by the controller (based on stability considerations) in different runs were between $1e-10$ s and $1e-8$ s. Seeing that the smallest period in these oscillations is on the order of $1e{-}3$ s, we believe this time scale is more than sufficient for temporal resolution of the problem.

All simulations were carried out until a limit cycle was reached, defined as the time when the growth rate of the pressure amplitude, taken between two consecutive cycles, is < 0.1%. The first three components in a Fourier series fit to the oscillating pressure were extracted from the transient results. Flow visualization, time and space averaging, and other post-processing tasks were performed using Paraview [47].

The heat exchangers were modelled as isothermal regions, with hydraulic radius and porosity identical to the stack. As such, they account for additional losses within their structure, but the heat transfer is only one-sided - within the resonator. We note that in the experimental system, the hydraulic radius of the heat exchangers was slightly different (up to 20% deviation), the porosity was significantly different due to the presence of water pipes, and the temperature was not necessarily uniform. Furthermore, the assumed linear temperature profile in the stack is not consistent with the actual temperature profile, which was determined by solid/fluid coupling in the stack region. As will be shown, these differences between experiment and simulation did not significantly affect the accuracy of our results.

The majority of the simulations used a 2D unstructured mesh, with local refinement in the stack region as well as in the boundary layer regions expected to form near the top and bottom walls (see Fig. 2 **(B)**). While the mesh itself appears rather coarse, the flux reconstruction approach used in PyFR makes use of internal solution points within the elements, leading to many more degrees of freedom (DOF) per variable compared to a standard finite volume method using the same number of elements. The solver was configured to use 3rd-order solution polynomials, resulting in 4th-order spatial accuracy. The resulting degrees of freedom of the mesh equals the element count multiplied by 16 for a 2D mesh using quadrangular elements and by 64 for a 3D mesh of Hexahedral elements. Validation simulations were performed on a refined mesh (mesh2) and on a 3D mesh. The 3D mesh was obtained by extruding the 2D mesh in the $z$-direction. Details of the different meshes can be found in Table 2. We note that extrusion of the mesh in the z direction is not an accurate representation of the actual 3D geometry in the experiments, in which the resonator was cylindrical, and the stack pores were hexagonal. However, it serves to investigate the importance of 3D effects on simulation accuracy.

Simulations were performed on 8 Nvidia A100 GPU cards. The 2D calculations took ~500 hours to reach a limit cycle from near-quiescent conditions, and ~48 hours to converge from a sinusoidal initial pressure distribution. The 3D calculations took ~300 hours to converge from a sinusoidal initial pressure distribution.

## 3. Results and discussion

In this section, we present Limit cycle results obtained from PyFR simulations, discuss their accuracy, and provide insight on non-linear mechanisms in the thermoacoustic engine. In all simulations, the temperature difference on the porous region was high enough to trigger a thermoacoustic instability. The acoustic pressure amplitude was observed to grow due to the thermoacoustic amplification, until the generated acoustic power is dissipated by various mechanisms, resulting in a limit cycle. Animated visualizations of flow, energy conversion and the growth of the disturbance are available in the supplementary material. As can be seen in Fig. 3 **A–B**, the temperature field in the limit cycle is indicative of vortical structures in the velocity field, interacting with the acoustic wave.

### 3.1. Validation

We begin by examining the pressure amplitude at the antinode, which will be used for validating the simulations against experimetal measurement made at that location in the resonator. Fig. 3 **(C)** displays the pressure amplitude obtained through calculations made using the three different meshes presented in Table 2. As can be seen, the results are in good agreement with each other, indicating that further mesh refinement is not required. The comparison to 3D results indicates that for this system, 2D simulations are sufficient for capturing the physical behaviour. We note that in this result, flow is strictly non-turbulent (a reduced Reynolds number of $\approx 1400$). In the presence of higher pressure amplitudes, the flow may become turbulent, requiring turbulence modelling or possibly direct 3D numerical simulation for accurate prediction.

Next, we validate the limit cycle calculations against results from the literature, using the pressure amplitude at the antinode as the basis for comparison. Fig. 4 **(A)** displays the transient growth of the pressure at the left end of the resonator. The last 10 cycles of the transient pressure were then fitted to a Fourier series, the first two terms of which are taken as the resonant mode, $p_1$, and the first harmonic, $p_2$, respectively. Fig. 4 shows the amplitude of $p_1$ and $p_2$ as a function of the hot side temperature, $T_H$. The results in the current work are shown alongside experimental results [20], calculations based on the linear model (applied in DeltaEC [12]), as well as calculations from the intermediate model of Abd El-Rahman and Abdel-Rahman [39]. As can be

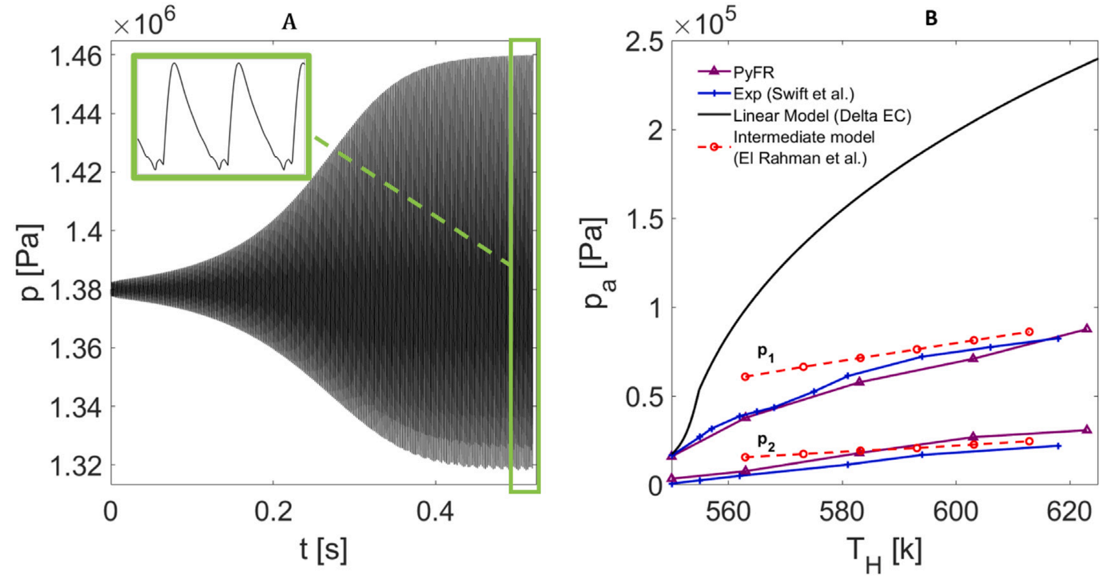


**Fig. 4.** **A:** The transient pressure at the end of the resonator grows until a limit cycle is reached. The limit cycle is highly non-linear, as can be seen in the indented figure. The pressure amplitude can be extracted from this limit cycle. **B:** Pressure amplitude obtained with the 2D PyFR computations, compared with the linear model [12], the intermediate model by Abd El-Rahman and Abdel-Rahman [39] based on the method of characteristics, and the experimental results by Swift [20]. Results obtained for the primary mode of the pressure are in excellent agreement with the experimental results, showing a maximum deviation < 10%).

seen, our results are in excellent agreement with the experimental data. By interpolating the numerical data at the experimental temperature points, we can obtain the deviation, resulting in a maximal deviation < 9%, and an average deviation < 5%. Results for the first harmonic are less accurate, with an average deviation of 23%. For both harmonics, results are, on average, more accurate compared to results obtained by other models. In contrast, the linear model is highly inaccurate, over-predicting the pressure amplitude by nearly a factor of 4 at higher temperatures. This inaccuracy is related to non-linear acoustic effects that attenuate the wave and contribute to saturation of the acoustic growth. Some of these effects will be discussed in subsequent sections. The obtained reduced frequency, $f L/a$, was 0.534, within < 1% of the experimental results. However, this result is unsurprising, as it is easy to accurately obtain the frequency with much simpler models including the linear model [20].

### 3.2. Rayleigh and jet streaming

We now turn to investigate the influence of non-linear effects on engine performance, beginning with acoustic streaming, which is an important non-linear effect occurring in thermoacoustic devices. While Gedeon Streaming occurs solely in looped, travelling wave systems, two forms of streaming exist in standing wave systems: Rayleigh Streaming and jet Streaming [19]. Rayleigh Streaming is related to boundary layer effects occurring near the walls, primarily with a temperature gradient on them. Due to the variation of fluid properties (most notably, viscosity) during the acoustic cycle, this leads to a preferential flow direction. Streaming in the boundary layer is countered by a returning flow, stemming further from the wall, in order to maintain a mass balance. Jet streaming relates to the asymmetry of the flow near the edge of the stack: When the flow exits the stack, it is driven out in jets, often with $y$ velocity-components. However, when the flow is returned towards the stack by the acoustic wave, it is returned into different pores. The net process in the acoustic cycle is manifested as mass streaming in both the $x$ and $y$ directions. This streaming is compensated for by mass circulation at other cross sections, thus maintaining a mass balance.

Net local streaming in several sections across the resonator is displayed in Fig. 5**(A)**, obtained by time-averaging the velocity over several cycles. Our simulation results indicate that in the majority of the resonator, Rayleigh streaming is dominant and is directed towards the pressure node, as expected based on known theory [19]. However, near the stack, jet streaming is found to be more dominant.

We note that, overall, the influence of these streaming velocities on the engine performance appears negligible. The time-averaged velocities are smaller than the oscillating velocity by nearly two orders of magnitude, and the heat fluxes associated with them are on the order of

$$Q_{Streaming} \approx u_{Streaming} c_p, \Delta T A \tag{15}$$

Where $u_{streaming}$ is the streaming velocity, and $A$ is the resonator area. Even under conservative assumptions (e.g $u_{streaming}$ = 0.01 m/s, $\Delta T$ = 600 K), the heat flux in [20]'s system is approximately 100 W, which is a small fraction of the total thermoacoustic heat flux, which can be up to 6000 W. Animations of the jet and Rayleigh streaming may be found in the supplementary material of this work.

### 3.3. Harmonics and their suppression

As the pressure amplitude grows, additional energy is transferred to other harmonics, leading to multi-frequency acoustic waves. Fig. 5 (C) displays the oscillating velocity, $u$, in the stack region, compared to the first term in the Fourier series, $u_1$. As seen by the effect of this single added term, the higher terms contribute significantly to the waveform, altering it.

The effect of higher harmonics on the acoustic wave has generally been considered negligible. [19,49]. However, in the experimental system itself [20] it was shown that the suppression of harmonics, by introduction of physical inserts into the resonator, greatly enhanced the pressure amplitude and improved agreement between the linear model and experimental measurements. Fig. 5 **(B)** shows the calculated relative value of the first harmonic, $g_2$, compared with the primary mode, $g_1$, for different oscillating properties inside the stack (i.e., velocity, pressure, temperature etc, designated in general as $g$). Results show that the amplitudes of higher harmonics in the stack are much larger than at the closed wall (for comparison, see the experimental and numerical results in Fig. 3 **(B)**). Indeed, the oscillating velocity exhibits the ratio $u_2/u_1 = 0.7$, which violates the single frequency assumption of the linear model. This deviation in the oscillating velocity leads to an even larger deviation for the local hydrodynamic heat flux $q = \rho c_p u T$.

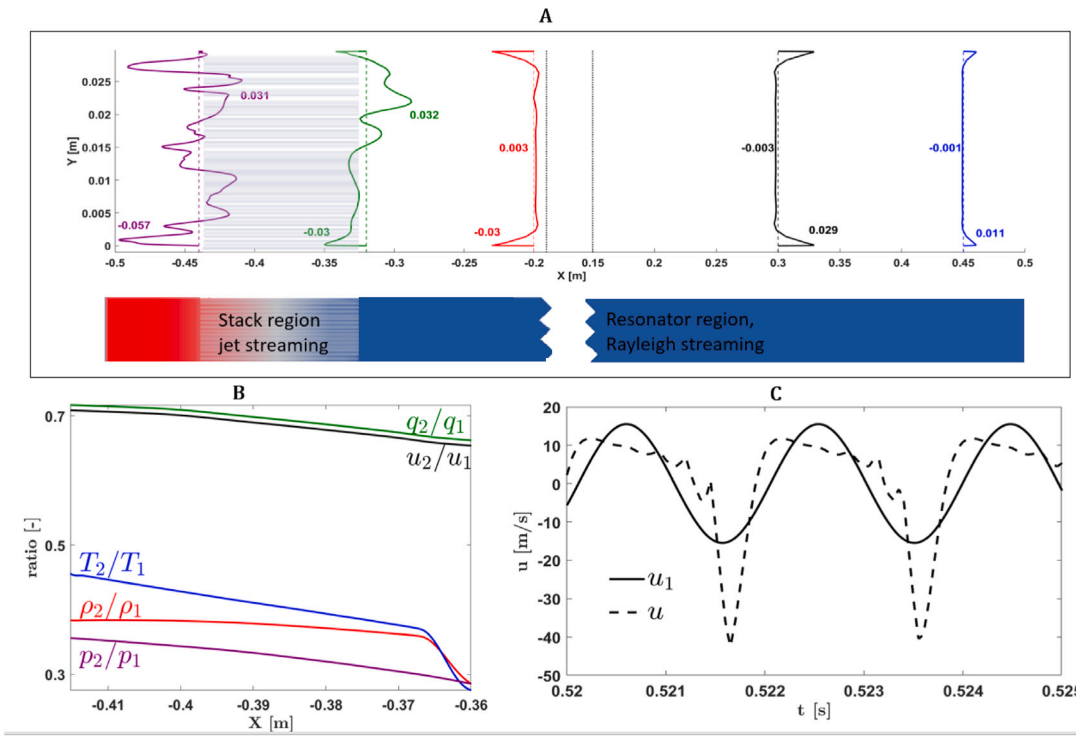


**Fig. 5.** Investigation of non-linear effects. **(A):** Time-averaged velocity distributions at various cross sections along the system. Rayleigh streaming dominates most of the resonator, with the exception of regions in proximity of the stack, where jet streaming is more prominent. **(B):** Harmonic content in the stack, computed using the ratio of the first mode $g_1$ and the first harmonic $g_2$, were $g$ represents any oscillating quantity (temperature, density, pressure, velocity or hydrodynamic heat flux). **(C):** The waveform of the full oscillating velocity, $u$, compared with the first mode $u_1$. i.e., the first term in the Fourier series. Results indicate a significant deviation of the waveform from the single-frequency approximation of the linear model.

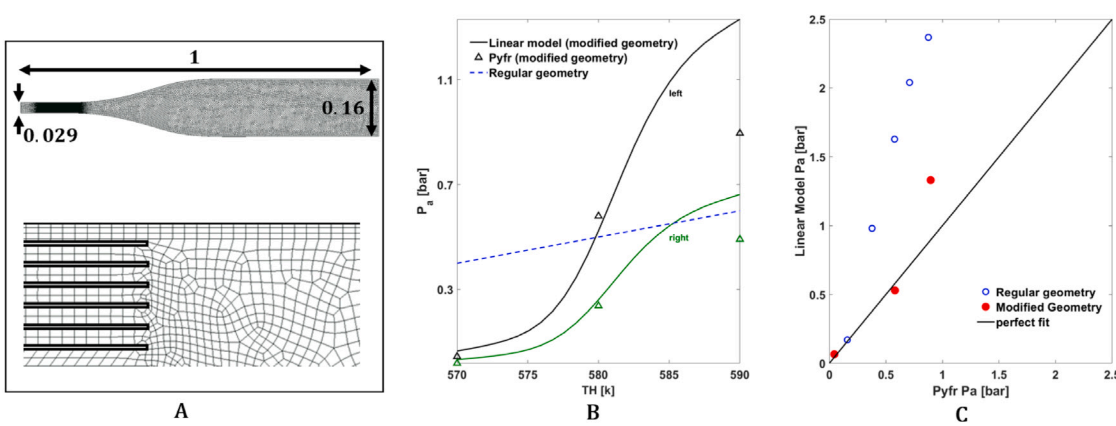


**Fig. 6.** Harmonic suppression. **(A):** Simulations of a model geometry based on [48], designed to suppress the harmonic content of the acoustic field. **(B):** The pressure amplitude, taken from the PyFR simulations and linear model calculations for this geometry, at the right and left ends of the resonator. The alternate geometry results in higher pressure amplitudes at the same temperatures. **(C):** comparison of PyFR results with the linear model for both the original and modified geometries. The harmonic suppression achieved by the alternate geometry greatly improves the agreement of the linear model with the PyFR results.

To further investigate the effect of harmonics on performance and agreement with the linear model, the system geometry was modified to a varying cross-section resonator, as described in Fig. 6 **(A)**. This geometry was taken from the work of Červenka et al. [48], who demonstrated its efficiency in suppressing higher harmonics. The numerical mesh size and elements remained similar to that in previous simulations. Simulations were run under identical conditions to those described previously and compared to results obtained from the linear model, calculated using PC-TAS [15]. Results indicate a much better agreement between the linear model and PyFR than obtained for the straight resonator geometry, with 45% maximal deviation (see Fig. 6**(B–C)**). Furthermore, the pressure amplitudes are significantly higher than the corresponding values, at the same temperatures, achieved with the simple, constant cross-section geometry. The increased amplitude of the resonant mode indicates better utilization of the produced power, due to harmonic suppression. Overall, these results clearly illustrate the importance of higher harmonics and highlight the need for accurate numerical methods that can capture these effects.

## 4. Conclusion

High-fidelity simulations of a thermoacoustic engine were conducted and shown to be in good agreement with experimental results. Further, the impact of non-linear effects within the engine was discussed and analysed. Specifically, the importance of harmonic content

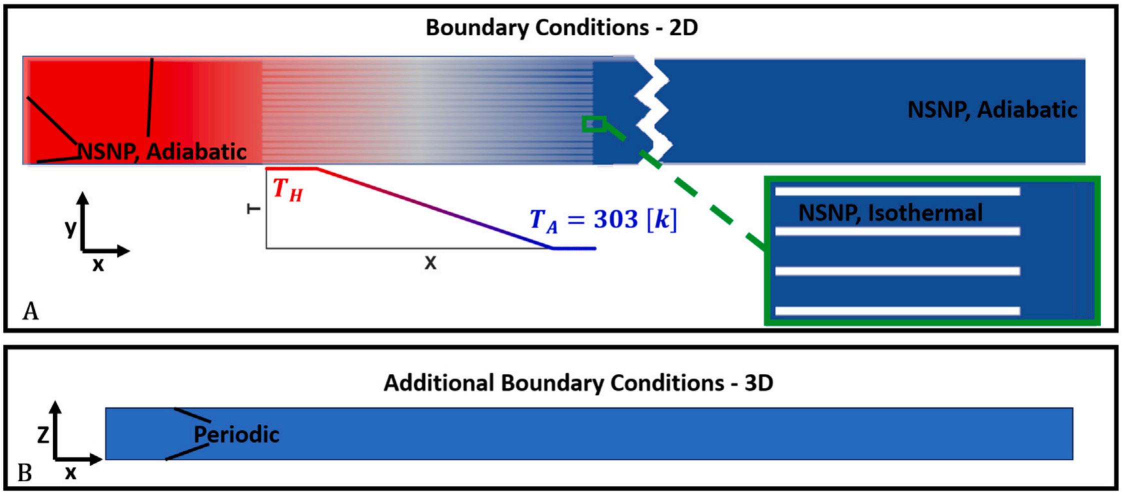


**Fig. A.1.** Boundary and Initial conditions. no slip, no penetration boundary conditions (NSNP) are imposed on all walls in the 2D simulation. periodic boundary conditions are imposed on the boundaries in the 3D simulation. Isothermal and Adiabatic conditions are imposed on the stack and resonator walls, respectively.

**Table A.1**
Initial conditions for two cases. $p_0$ was chosen so that it would be near the predicted pressure amplitude, in order to accelerate the convergence of the simulation. The initial temperature profile was as described in Fig. A.1.

| Case | Pressure distribution | Velocity distribution |
|---|---|---|
| Near quiescent conditions (One simulation) | $p = p_m$ | $u = 0.1$ [m/s] |
| Most simulations | $p = p_m + p_0 sin(\pi x)$ | $u = 0$ |

in the generated acoustic field, often considered negligible, was illustrated via a resonator geometry aimed at suppressing higher harmonics. The simulations showed how such geometric suppression improved performance and resulted in better agreement with linear theory, where harmonics are unaccounted for.

Future work should target the development of additional models that accurately capture thermoacoustic phenomena, including transient 1D models, turbulence models tailored for acoustics, or correction terms to the existing linear model. CFD-based results can be used to tune the parameters for these models, with the goal of obtaining accurate and computationally efficient models. Further extensions should be made for the simulation of additional geometries and additional physics.

Due to their highly efficient performance, travelling wave engines are a natural target for future simulations in PyFR. The key additional challenge is the regenerator section, as the pores are typically an order of magnitude smaller, and the structure is not ordered. Two possible modelling approaches could be: (1) direct resolution of the pores with a simplified geometry, or (2) modelling the porous region as a source term in the momentum equation and energy equation.

As stated previously, both 2D and 3D simulations conducted here do not fully represent the complex geometry and multi-physics coupling present in the experimental device. More accurate simulations can be achieved by fully accounting for the geometry of the stack and heat-exchangers, the circular geometry of the resonator, the solid conduction in the porous region, and the heat exchange with the environment. The latter could be modelled by coupling the solver with a 0th or 1st order model for the heat exchanger. It stands to reason that a full three-dimensional simulation with additional physics would likely result in an even more accurate prediction, but with substantially higher computational cost.

## CRediT authorship contribution statement

**Nathan Blanc:** Writing – original draft, Visualization, Validation, Software, Methodology, Investigation, Conceptualization. **Michael Laufer:** Writing – review & editing, Visualization, Software. **Steven Frankel:** Writing – review & editing, Resources, Methodology. **Guy Z. Ramon:** Writing – review & editing, Supervision, Methodology, Conceptualization.

## Declaration of competing interest

The authors declare that they have no known competing financial interests or personal relationships that could have appeared to influence the work reported in this paper.

## Data availability

Data will be made available on request.

## Acknowledgements

This work was supported by the Israel Ministry of Energy and Infrastructure, grant 219-11-127. N.B would like to thank the Grand Technion Energy Program (GTEP) and the Jacobs fellowship for their support.

## Appendix A

### *A.1. Boundary and initial conditions*

In this appendix, we give the details of the initial and boundary conditions in the form of a figure and table. Initial conditions are displayed in Table A.1 and boundary conditions are displayed in Fig. A.1.

### *A.2. Previous studies employing full-scale CFD*

In this Appendix we review previous full scale CFD studies of thermoacoustic devices in detail. Di Meglio and Massarotti [21] published a comprehensive and detailed review of previous simulations. Herein we discuss all the relevant papers reviewed by them and a few additional ones. The papers are listed in Table A.2, as well as the device modelled, the numeric tool used, and notes about model validation. as can be seen in the table, no previous study has obtained good agreement with experimental results for a full scale CFD simulation of a thermoacoustic device operating at a drive ratio bigger than 5%. The vast majority of the studies reviewed use commercial tools, which are possibly not accurate enough to properly capture the complex couplings in thermoacoustic devices.

**Table A.2**
List of previous full scale CFD simulations of thermoacoustic devices.

| Reference | System | Numerical methodology | High fidelity? | Validated? | Notes |
|---|---|---|---|---|---|
| Chen et al. [28] | Standing Wave Engine | ANSYS Fluent 2D | no | Against Linear Model | |
| Zhang et al. [50] | Standing Wave Engine | In House Simple Algorithm | no | Against Linear Model | |
| Luo et al. [26] | Standing wave engine Coupled with liquid Piston | Transient 2D CFD Coupled With Impedance Model | no | Against Experiment | Low Amplitudes, Linear Model Valid |
| Yu et al. [23] | Standing Wave Engine | ANSYS Fluent 2D | no | yes | Poor Agreement at Higher Amplitudes |
| Chen et al. [51] | Standing Wave Engine | ANSYS Fluid LES | yes | no | |
| Lycklama à Nijeholt et al. [52] | Travelling Wave Engine | CFX4.4 | no | no | |
| Lin et al. [32] | Piezo-coupled Standing Wave Engine | CharLES | yes | Against Linear Model | |
| Scalo et al. [31] | Travelling Wave Engine | CharLES | yes | no | |
| Uzay et al. [53] | Standing Wave Couple | COMSOL Multiphysics | no | Against other CFD | |
| Cao et al. [54] | Standing Wave Couple | SOLA ICE | no | no | |
| Ali et al. [55] | Travelling Wave Engine | COMSOL Multiphysics | no | no | |
| Tasnim and Fraser [56] | Standing Wave Refrigerator | OpenFoam | no | Against other CFD | |
| Skaria et al. [24] | Standing Wave Couple & Travelling Wave Engine | Not Fully Stated | no | Against Experiment | Poor Agreement |
| Sharify et al. [25] | Loudspeaker Driven Refrigerator | In House Code | no | Against Experiment | Low Amplitudes, Linear Model Valid |
| Yu et al. [22] | Travelling Wave Engine | ANSYS Fluent 2D | no | Against Experiment | Poor Agreement |
| Yang et al. [57] | Travelling Wave Engine | In House PISO | no | no | |
| Zink et al. [58]<br>Zink et al. [58] | Standing Wave Engine<br>Standing Wave Engine | ANSYS Fluent 2D<br>ANSYS Fluent 2D | no<br>no | no<br>no | |
| Zink et al. [29] | Standing Wave Engine | ILES | yes | no | |
| Zhang et al. [59] | Standing Wave Couple | ANSYS Fluent 2D | no | no | |
| Bouramdane et al. [60] | Standing Wave Couple | COMSOL Multiphysics | no | no | |
| Chen et al. [61] | Coupled Thermoacoustic Engines | ANSYS Fluent 2D | no | no | |
| Rogoziński and Nowak [62] | Coupled Thermoacoustic Engines | ANSYS Fluent 2D | no | no | |
| Guo et al. [63] | Standing Wave Engine | ANSYS Fluent LES | yes | Against other CFD | |
| Gupta et al. [64] | Standing Wave Couple | ANSYS Fluent 2D | no | no | |
| Kuzuu and Hasegawa [65] | Standing Wave Engine | LS-FLOW (In House) | no | Against Linear Model | |
| Kuzuu and Hasegawa [66] | Standing Wave Engine | LS-FLOW (In House) | no | Against Linear Model | |
| Harikumar et al. [27] | Standing Wave Engine | ANSYS Fluent 2D | no | Against Experiment | Low Amplitudes, Linear Model Valid |
| Tisovsky and Vit [67] | Loudspeaker Driven Refrigerator | OpenFoam | no | no | |
| Chen et al. [68] | Standing Wave Engine | ANSYS Fluent 2D | no | Against Linear Model | |
| Liu et al. [69] | Standing Wave Engine | ANSYS Fluent 2D | no | Against Linear Model | |
| Miled et al. [70] | Standing Wave Couple | In House Code | no | Against other CFD | |
| Liu et al. [71] | Standing Wave Engine | ANSYS Fluent 2D | no | Against Linear Model | |
| Guo et al. [30] | Standing Wave Engine | ANSYS Fluent 3D including LES | yes | Against other CFD | |

## Appendix B. Supplementary material

Supplementary material related to this article can be found online at https://doi.org/10.1016/j.apenergy.2024.122817. Supplementary material includes videos, visualising the Simulation results and the concepts discussed in this paper.

## References


[1] Bi T, Wu Z, Zhang L, Yu G, Luo E, Dai W. Development of a 5kW traveling-wave thermoacoustic electric generator. Appl Energy 2017;185:1355–61, Clean, Efficient and Affordable Energy for a Sustainable Future.

[2] Wang K, Sun D, Xu Y, Zou J, Zhang X, Qiu L. Operating characteristics of thermoacoustic compression based on alternating to direct gas flow conversion. Energy 2014;75:338–48.

[3] Yang Y, Chi J, Wu Z, Yang R, Xu J, Zhang L, et al. A heat-driven combined cooling and heating system based on thermoacoustic technology. Appl Phys Lett 2022;120(22):223902.

[4] Xu J, Luo E, Hochgreb S. A thermoacoustic combined cooling, heating, and power (CCHP) system for waste heat and LNG cold energy recovery. Energy 2021;227:120341.

[5] Zhang X, Chang J. Onset and steady-operation features of low temperature differential multi-stage travelling wave thermoacoustic engines for low grade energy utilization. Energy Convers Manage 2015;105:810–6.

[6] Wright G, Wright D, Goodson G, Rieke G, Kroes G, Amiaux J, et al. The mid-infrared instrument for the James Webb space telescope, II: Design and build. Publ Astron Soc Pac 2015;127.

[7] Wollan JJ, Swift GW, Backhaus SN, Gardner DL. Development of a thermoacoustic natural gas liquefier. 2002.

[8] de Blok K. Novel 4-stage traveling wave thermoacoustic power generator. In: Fluids engineering division summer meeting, ASME 2010 3rd Joint US-European Fluids Engineering Summer Meeting: Volume 2, Fora, 2010, p. 73–9.

[9] Bou Nader W, Chamoun J, Dumand C. Thermoacoustic engine as waste heat recovery system on extended range hybrid electric vehicles. Energy Convers Manage 2020;215:112912.

[10] Rott N. Thermally driven acoustic oscillations. Part II: Stability limit for helium. Z Angew Math Phys ZAMP 1973;24(1):54–72.

[11] Swift GW. Thermoacoustic engines. J Acoust Soc Am 1988;84(4):1145–80.

[12] Ward B, Clark J, Swift G. DELTAEc version 6.2: Users guide. Los Alamos National Laboratory; 2008.

[13] Yazaki T, Iwata A, Maekawa T, Tominaga A. Traveling wave thermoacoustic engine in a looped tube. Phys Rev Lett 1998;81:3128–31. http://dx.doi.org/10.1103/PhysRevLett.81.3128, URL https://link.aps.org/doi/10.1103/PhysRevLett.81.3128.

[14] Curtis SB. Modification and vErification of Design Simulation for Thermoacoustic Research Software. Technical Report, NAVAL POSTGRADUATE SCHOOL MONTEREY CA; 2000.

[15] Yang R, Blanc N, Vardi-Chouchana A, Ouzana N, Ramon GZ. PC-TAS: A design environment for phase-change and classical thermoacoustic systems. SoftwareX 2022;19:101142. http://dx.doi.org/10.1016/j.softx.2022.101142, URL https://www.sciencedirect.com/science/article/pii/S2352711022000899.

[16] Raspet R, Slaton WV, Hickey CJ, Hiller RA. Theory of inert gas-condensing vapor thermoacoustics: Propagation equation. J Acoust Soc Am 2002;112(4):1414–22.

[17] Slaton WV, Raspet R, Hickey CJ, Hiller RA. Theory of inert gas-condensing vapor thermoacoustics: Transport equations. J Acoust Soc Am 2002;112(4):1423–30.

[18] Yang R, Blanc N, Ramon GZ. Environmentally-sound: An acoustic-driven heat pump based on phase change. Energy Convers Manage 2021;232:113848.

[19] Swift G. Thermoacoustics - A unifying perspective for some engines and refrigerators. Springer; 2002.

[20] Swift GW. Analysis and performance of a large thermoacoustic engine. J Acoust Soc Am 1992;92(3):1551–63.

[21] Di Meglio A, Massarotti N. CFD modeling of thermoacoustic energy conversion: A review. Energies 2022;15(10):3806.

[22] Yu G, Luo E, Dai W, Hu J. Study of nonlinear processes of a large experimental thermoacoustic-stirling heat engine by using computational fluid dynamics. J Appl Phys 2007;102(7):074901.

[23] Yu G, Dai W, Luo E. CFD simulation of a 300Hz thermoacoustic standing wave engine. Cryogenics 2010;50(9):615–22, 2009 Space Cryogenic Workshop.

[24] Skaria M, Rasheed KA, Shafi K, Kasthurirengan S, Behera U. Simulation studies on the performance of thermoacoustic prime movers and refrigerator. Comput & Fluids 2015;111:127–36.

[25] Sharify EM, Takahashi S, Hasegawa S. Development of a CFD model for simulation of a traveling-wave thermoacoustic engine using an impedance matching boundary condition. Appl Therm Eng 2016;107:1026–35.

[26] Luo J, Zhou Q, Jin T. Numerical simulation of nonlinear phenomena in a standing-wave thermoacoustic engine with gas-liquid coupling oscillation. Appl Therm Eng 2022;207:118131.

[27] Harikumar G, Shen L, Wang K, Dubey S, Duan F. Transient thermofluid simulation of a hybrid thermoacoustic system. Int J Heat Mass Transfer 2022;183:122181.

[28] Chen G, Tang L, Mace BR. Bistability and triggering in a thermoacoustic engine: A numerical study. Int J Heat Mass Transfer 2020;157:119951.

[29] Zink F, Vipperman J, Schaefer L. CFD simulation of a thermoacoustic engine with coiled resonator. Int Commun Heat Mass Transfer 2010;37(3):226–9.

[30] Guo L, Zhao D, Xu J, Tokhi MO, Karimi HR. Predicting unsteady heat-fluid interaction features and nonlinear acoustic behaviors in standing-wave thermoacoustic engines using unsteady RANS, LES and hybrid URANS/LES methods. Int Commun Heat Mass Transfer 2023;142:106617.

[31] Scalo C, Lele SK, Hesselink L. Linear and nonlinear modelling of a theoretical travelling-wave thermoacoustic heat engine. J Fluid Mech 2015;766:368–404.

[32] Lin J, Scalo C, Hesselink L. High-fidelity simulation of a standing-wave thermoacoustic–piezoelectric engine. J Fluid Mech 2016;808:19–60.

[33] GEDEON D. A globally-implicit stirling cycle simulation. 1986.

[34] Gary J, O'Gallagher A, Radebaugh R. A numerical model for regenerator performance. Boulder (CO): National Institute of Standards and Technology; 1994.

[35] Ahmed F, Yu G, Luo E. Multi-method modeling to predict the onset conditions and resonance of the piezo coupled thermoacoustic engine. J Acoust Soc Am 2022;151(6):4180.

[36] Boroujerdi A, Ziabasharhagh M. Investigation of a high frequency pulse tube cryocooler driven by a standing wave thermoacoustic engine. Energy Convers Manage 2014;86:194–203.

[37] Sugimoto N. Thermoacoustic effects on the propagation of non-planar sound in a circular duct. J Fluid Mech 2022;945:A26. http://dx.doi.org/10.1017/jfm.2022.523.

[38] Olivier C, Penelet G, Poignand G, Gilbert J, Lotton P. Weakly nonlinear propagation in thermoacoustic engines: A numerical study of higher harmonics generation up to the appearance of shock waves. Acta Acustica United Acustica 2015;101(5):941–9.

[39] Abd El-Rahman AI, Abdel-Rahman E. Characteristic-based non-linear simulation of large-scale standing-wave thermoacoustic engine. J Acoust Soc Am 2014;136(2):649–58.

[40] Boroujerdi AA, Ziabasharhagh M. A coupled computational model of non-linear thermoacoustics of standing wave heat engines. Heat Mass Transf 2019;55(11):3223–41.

[41] Olson J, Swift G. Similitude in thermoacoustics. J Acoust Soc Am 1994;95(3):1405–12.

[42] Witherden FD, Farrington AM, Vincent PE. PyFR: An open source framework for solving advection–diffusion type problems on streaming architectures using the flux reconstruction approach. Comput Phys Comm 2014;185(11):3028–40.

[43] Huynh HT. A flux reconstruction approach to high-order schemes including discontinuous Galerkin methods. In: 18th AIAA computational fluid dynamics conference. http://dx.doi.org/10.2514/6.2007-4079, URL https://arc.aiaa.org/doi/abs/10.2514/6.2007-4079, arXiv:https://arc.aiaa.org/doi/pdf/10.2514/6.2007-4079.

[44] Trojak W, Vincent P. An extended range of energy stable flux reconstruction methods on triangles. J Sci Comput 2023;96(1):32.

[45] Vermeire BC, Witherden FD, Vincent PE. On the utility of GPU accelerated high-order methods for unsteady flow simulations: A comparison with industry-standard tools. J Comput Phys 2017;334:497–521.

[46] Sutherland W. LII. The viscosity of gases and molecular force. Lond, Edinb, Dublin Philos Mag J Sci 1893;36(223):507–31.

[47] Ahrens J, Geveci B, Law C. Paraview: An end-user tool for large data visualization. In: The visualization handbook, vol. 717, (no. 8). 2005.

[48] Červenka M, Šoltés M, Bednařík M. Optimal shaping of acoustic resonators for the generation of high-amplitude standing waves. J Acoust Soc Am 2014;136(3):1003.

[49] Chen G, Tang L, Mace B, Yu Z. Multi-physics coupling in thermoacoustic devices: A review. Renew Sustain Energy Rev 2021;146:111170.

[50] Zhang D, He Y, Wang Y, Huang J. Simulation of a standing-wave thermoacoustic engine using compressible SIMPLE algorithm. AIP Conf Proc 2010;1207(1):939–44. http://dx.doi.org/10.1063/1.3366490.

[51] Chen G, Wang Y, Tang L, Wang K, Mace B. Large eddy simulation of self-excited acoustic oscillations in a thermoacoustic engine. 2019.

[52] Lycklama à Nijeholt JA, Tijani MEH, Spoelstra S. Simulation of a traveling-wave thermoacoustic engine using computational fluid dynamics. J Acoust Soc Am 2005;118(4):2265–70. http://dx.doi.org/10.1121/1.2035567.

[53] Uzay BN, Yıldırım E, Turkoglu H. Numerical study on effects of computational domain length on flow field in standing wave thermoacoustic couple. Cryogenics 2019;98:139–47.

[54] Cao N, Olson J, Swift G, Chen S. Energy flux density in a thermoacoustic couple. J Acoust Soc Am 1996;99(6):3456–64.

[55] Ali MM, Martaj N, Laaouatni A, Savarese S, Bennacer R, Kouidri S. 2D simulation of the oscillating flow in the thermoacoustic engine Swift Backhaus. In: 2016 international renewable and sustainable energy conference. IEEE; 2016, p. 862–5.

[56] Tasnim SH, Fraser RA. Computation of the flow and thermal fields in a thermoacoustic refrigerator. Int Commun Heat Mass Transfer 2010;37(7):748–55.

[57] Yang P, Chen H, Liu Y. Numerical investigation on nonlinear effect and vortex formation of oscillatory flow throughout a short tube in a thermoacoustic stirling engine. J Appl Phys 2017;121(21):214902.

[58] Zink F, Vipperman JS, Schaefer LA. Advancing thermoacoustics through CFD simulation using FLUENT. In: ASME international mechanical engineering congress and exposition, vol. 48692, 2008, p. 101–10.

[59] Zhang Y, Shi X, Li Y, Zhang Y, Liu Y. Characteristics of thermoacoustic conversion and coupling effect at different temperature gradients. Energy 2020;197:117228.

[60] Bouramdane Z, Hafs H, Bah A, Alaoui M, Martaj N, Savarese S. Standing wave thermoacoustic refrigerator: The principle of thermally driven cooling. In: 2018 6th international renewable and sustainable energy conference. IEEE; 2018, p. 1–6.

[61] Chen G, Li Z, Tang L, Yu Z. Mutual synchronization of self-excited acoustic oscillations in coupled thermoacoustic oscillators. J Phys D: Appl Phys 2021;54(48):485504.

[62] Rogoziński K, Nowak G. Numerical investigation of dual thermoacoustic engine. Energy Convers Manage 2020;203:112231.

[63] Guo L, Zhao D, Becker S. Temperature difference and stack plate spacing effects on thermodynamic performances of standing-wave thermoacoustic engines driven by cryogenic liquids and waste heat. J Therm Sci 2022;1–18.

[64] Gupta S, Ghosh P, Nandi T. Theoretical and CFD investigations on a 200 Hz thermoacoustic heat engine using pin array stack for operations in a pulse tube cryocooler. In: IOP conference series: Materials science and engineering, vol. 502, (no. 1):IOP Publishing; 2019, 012025.

[65] Kuzuu K, Hasegawa S. Effect of non-linear flow behavior on heat transfer in a thermoacoustic engine core. Int J Heat Mass Transfer 2017;108:1591–601.

[66] Kuzuu K, Hasegawa S. Numerical investigation of heated gas flow in a thermoacoustic device. Appl Therm Eng 2017;110:1283–93.

[67] Tisovsky T, Vit T. Design of numerical model for thermoacoustic devices using OpenFOAM. In: AIP conference proceedings, vol. 1889, (1):AIP Publishing LLC; 2017, 020043.

[68] Chen G, Hao H, Deng A. Linear and nonlinear modeling of self-excited acoustic oscillations in a T-shaped thermoacoustic engine. AIP Adv 2021;11(8):085120.

[69] Liu L, Liu Y, Duan F. Effect of the characteristic time on the system performance of a three-stage looped traveling-wave thermoacoustic engine. Energy Convers Manage 2020;224:113367.

[70] Miled O, Dhahri H, Mhimid A. Numerical investigation of porous stack for a solar-powered thermoacoustic refrigerator. Adv Mech Eng 2020;12(6):1687814020930843.

[71] Liu L, Yang P, Liu Y. Comprehensive performance improvement of standing wave thermoacoustic engine with converging stack: Thermodynamic analysis and optimization. Appl Therm Eng 2019;160:114096.